Shapes of fluid membranes with chiral edges

Lijie Ding [1,*] Robert A. Pelcovits [1,2] and Thomas R. Powers [1,3]

[1]*Department of Physics, Brown University, 182 Hope Street, Providence, Rhode Island 02912, USA*

[2]*Brown Theoretical Physics Center and Department of Physics, Brown University, 182 Hope Street, Providence, Rhode Island 02912, USA*

[3]*Center for Fluid Mechanics and Department of Physics, Brown University, 182 Hope Street, Providence, Rhode Island 02912, USA*

(Received 22 April 2020; revised 15 July 2020; accepted 25 August 2020; published 14 September 2020)

We carry out Monte Carlo simulations of a colloidal fluid membrane with a free edge and composed of chiral rodlike viruses. The membrane is modeled by a triangular mesh of beads connected by bonds in which the bonds and beads are free to move at each Monte Carlo step. Since the constituent viruses are experimentally observed to twist only near the membrane edge, we use an effective energy that favors a particular sign of the geodesic torsion of the edge. The effective energy also includes the membrane bending stiffness, edge bending stiffness, and edge tension. We find three classes of membrane shapes resulting from the competition of the various terms in the free energy: branched shapes, chiral disks, and vesicles. Increasing the edge bending stiffness smooths the membrane edge, leading to correlations among the membrane normals at different points along the edge. The normalized power spectrum for edge displacements shows a peak with increasing preferred geodesic torsion. We also consider membrane shapes under an external force by fixing the distance between two ends of the membrane and finding the shape for increasing values of the distance between the two ends. As the distance increases, the membrane twists into a ribbon, with the force eventually reaching a plateau.

DOI: 10.1103/PhysRevE.102.032608

I. INTRODUCTION

Fluid membranes are ubiquitous in biological systems and exhibit various shapes due to their fluidity and the constraints of a fixed area and fixed volume. While closed membrane vesicles show a wide range of shapes including pears, discocytes, stomatocytes, and toroids [1], membranes with free edges can form shapes other than flat disks. For example, colloidal membranes composed of aligned rodlike chiral viruses in the presence of a polymer depletant are typically found to have open edges and form twisted ribbon shapes. The handedness of a ribbon, defined by the handedness of the helical edge of the ribbon, is determined by the intrinsic chirality of the viruses; reversing the chirality of the viruses reverses the handedness of the ribbons [2–4]. Lipid bilayer membranes with free edges also play a role during the formation of vesicles [5–7] and can be stabilized by reducing the line tension of the edge [8,9]. Likewise, liposomes exposed to increasing levels of the protein talin form liposomes with stable holes, cup-shaped liposomes, and, finally, lipid bilayer sheets [10,11]. Helical ribbons are also seen as intermediate states in the formation of self-assembled tubes from lipid molecules [12,13].

In this paper, we use Monte Carlo (MC) simulations to study the configurations that arise in a simple effective model for colloidal membranes. A theoretical model of the mechanics of colloidal membranes must account for the bending energy of the membrane, the chiral liquid crystal energy associated with the orientational ordering of the rodlike colloidal particles, and, finally, the energy associated with the free edges of the membrane. Models that have been developed to date include phenomenological Landau models [14–17], entropically motivated models [18,19], and hard-body simulations [20,21].

There are two competing effects governing the alignment of the rodlike viruses in a colloidal membrane. One is the tendency for the rods to line up side by side. The other is a tendency for the rods to twist due to their intrinsic chirality. These two tendencies are incompatible and thus the twist is confined to a region near the membrane edge. The thickness of this region is known as the twist penetration depth [22]. If the twist penetration depth is small compared to the lateral dimensions of the membrane, as is often the case in these colloidal membranes, the liquid crystalline degrees of freedom can be accounted for by an effective theory in which the local degrees of freedom do not appear explicitly, and the energy depends only on the geometric properties of the surface. This approach was taken by Jia *et al.* [17], who accounted for the liquid crystalline degrees of freedom with an effective edge energy which includes an edge tension term involving the length of the perimeter, a bending energy cost for the curvature of the edge, and a chiral term involving the geodesic torsion of the edge. The geodesic torsion is the rate that the normal to the surface twists around the edge of the surface [23]. Even when using this simplified model it is difficult, if not impossible, to analytically predict the equilibrium shapes of the membranes. Instead, specific shapes must be assumed and then the theory can assess which of those shapes will be energetically favorable. A more comprehensive theory would predict *a priori* the shape of the membrane given parameters such as the depletant concentration and virus chirality.

*lijie_ding@brown.edu

In this article, we take an important step towards developing such a comprehensive theoretical approach by carrying out MC simulations of a discrete version of the continuum model used by Jia *et al.* [17]. In our discrete model, the membrane is a triangular network consisting of hard spherical beads connected together by bonds [24,25]. Fluidity of the membrane is imposed by allowing for bond reconnections [26]. We first determine the topology changes of nonchiral membranes, recapitulating the results in Ref. [5], which include MC simulations showing a first-order transition from a branched-polymer shape to a closed vesicle at a low bending stiffness, as well as theoretical arguments indicating a transition from flat disks to closed vesicles at a higher bending stiffness. With greater computational power we are able to extend the simulation results of Ref. [5] to higher values of the membrane bending stiffness and study the transition from flat disks to closed vesicles.

Then we consider the effects of chirality on the membrane shape, both in the interior and on the edge. Finally, inspired by the experiments in Refs. [3] and [27], where colloidal membranes were stretched using optical tweezers, we fix the locations of two beads on opposite sides of the membrane and measure the energy of the system as the distance between these two beads is varied. From this energy we can deduce the force needed to stretch the membrane and compare our results qualitatively to the experimentally measured values.

II. CONTINUUM MODEL

The continuum model used by Jia *et al.* [17] is given by the following Hamiltonian, consisting of a bending term integrated over the area of the membrane and an edge term integrated over the perimeter:

$$\mathcal{H} = \mathcal{H}_b + \mathcal{H}_e. \tag{1}$$

The bending energy $\mathcal{H}_b$ is the Canham-Helfrich energy [28,29],

$$\mathcal{H}_b = \int dA\left[\frac{\kappa}{2}(2H)^2 + \bar{\kappa}K\right], \tag{2}$$

where κ is the bending modulus, $H = (1/R_1 + 1/R_2)/2$ is the mean curvature, $\bar{\kappa}$ is the Gaussian curvature modulus, $K = 1/(R_1R_2)$ is the Gaussian curvature, and R_1 and R_2 are the two principal radii of curvature of the surface.

The modulus $\bar{\kappa}$ is of the order of hundreds of k_BT [17,19] and κ is of the order of 10 000 k_BT [30]. The effective edge energy $\mathcal{H}_e$ proposed by Jia *et al.* is given by

$$\mathcal{H}_e = \oint ds\left[\lambda + \frac{B}{2}k^2 + \frac{B'}{2}(\tau_g - \tau_g^*)^2\right], \tag{3}$$

where λ is the line tension, B is the edge bending stiffness, and k is the curvature of the edge. The effect of chirality is introduced in the last term of the above equation with the edge torsional modulus B' and the geodesic torsion $\tau_g = \hat{\mathbf{T}} \cdot (\hat{\mathbf{n}}_c \times d\hat{\mathbf{n}}_c/ds)$. The geodesic torsion is the rate of rotation of the surface normal $\hat{\mathbf{n}}_c$ around the tangent $\hat{\mathbf{T}}$ of the edge [23,31]. The parameter τ_g^* is the spontaneous geodesic torsion of the edge and represents the chirality of the constituent virus particles which comprise the membrane. The sign of τ_g^* is determined by the chirality of the particles.

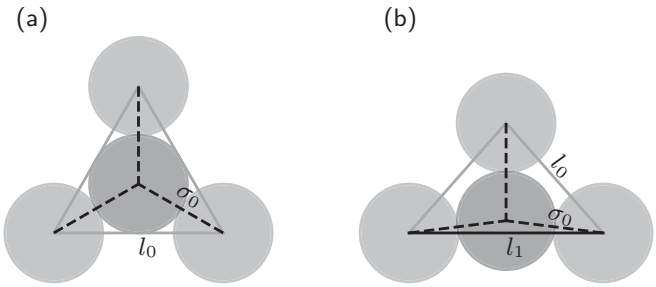

FIG. 1. Maximum bond lengths for self-avoidance of the membrane. The figures show a triangle of beads (a) in the interior and (b) at the edge of the membrane. Self-avoidance means that the fourth bead cannot pass through the triangle. The figures show the threshold for self-avoidance, i.e., the fourth bead could pass through if any of the bond lengths are increased. The dashed line joins the center of the fourth bead and any of the centers of the beads forming the triangle and has length σ_0, the diameter of a bead. (a) We see that l_0, the maximum length of a bond in the membrane interior, is given by $l_0 = \sqrt{3}\sigma_0$. (b) In the obtuse triangle at the membrane edge the edge bond (horizontal line) has length l_1, the maximum possible value for an edge bond, while the other two sides of the triangle have length l_0, the maximum length for interior bonds. From the figure we deduce that $l_1 = l_0\sqrt{4 - l_0^2/\sigma_0^2}$.

III. DISCRETE MODEL

We discretize the model in the previous section using a bond-and-bead model for self-avoiding membranes [24]. The continuous two-dimensional membrane surface is replaced by a triangular mesh $\mathcal{M}$ with hard-sphere beads of diameter σ_0 on vertices of the mesh which are connected by bonds. Each bead can be thought of as a coarse-grained group of virus particles. A bond connecting two beads does not allow them to move farther apart than a distance l_0 for interior bonds and l_1 for edge bonds. We choose $l_1 > l_0$, so that triangles at the membrane edge are more obtuse than those in the interior of the membrane. If the triangles at the edge of the membrane are too acute, the removal of an edge bond would be prohibited because it would require a large edge bending cost. With $l_1 > l_0$ we avoid this problem. For beads separated by a distance less than l_0 in the interior and less than l_1 at the edge (but greater than σ_0 because of the beads' hard cores), we assume that there is no interaction between the beads, even when they are connected by bonds. To avoid self-intersection of the membrane where one bead might pass through the center of a triangle formed by three other beads, we require that $l_0 < \sqrt{3}\sigma_0$ and $l_1 < l_0\sqrt{4 - l_0^2/\sigma_0^2}$ (see Fig. 1).

The energy of a configuration of beads and bonds is given by discretizing Eqs. (2) and (3), subject to the constraints imposed by the hard cores of the beads and the presence of bonds. For all but the last term in Eq. (3), we use discretized forms of the terms appearing in the total energy Eq. (1) that have appeared previously in the literature. The discretized mean curvature $H(i)$ at bead i is [24,32–35]

$$H(i) = \frac{1}{2\sigma_i}\hat{\mathbf{n}}(i) \cdot \sum_{j(i)} \frac{d_{ij}}{l_{ij}}(\vec{\mathbf{r}}_i - \vec{\mathbf{r}}_j), \tag{4}$$

where the sum is over the neighbors $j(i)$ of bead i, and $\hat{\mathbf{n}}(i)$ is the surface normal at bead i. The surface normal at bead i is defined as [36]

$$\hat{\mathbf{n}}(i) = \frac{\sum_j \theta_j \hat{\mathbf{n}}_j}{|\sum_j \theta_j \hat{\mathbf{n}}_j|}, \tag{5}$$

where the sum is over all of the triangles with one vertex at i, $\hat{\mathbf{n}}_j$ is the direction normal to the jth triangle, and θ_j is the interior angle of triangle j at vertex i. The distance between bead i and bead j is $l_{ij} = |\vec{\mathbf{r}}_i - \vec{\mathbf{r}}_j|$, where $\vec{\mathbf{r}}_i$ is the position vector of bead i. The length d_{ij} is given by $d_{ij} = l_{ij}(\cot\theta_1 + \cot\theta_2)/2$, where θ_1 and θ_2 are the angles opposite bond ij in the two triangles which meet at the bond, and $\sigma_i = \sum_{j(i)} d_{ij} l_{ij}/4$ is the area of the cell on the virtual dual lattice centered at bead i. See Ref. [35] for a detailed explanation of this discretized mean curvature. Since calculating $H(i)$ requires that every bond connecting to i has two neighboring triangles, which is not satisfied for an edge bond, we only include beads in the membrane interior when calculating the bending energy. The integral of Gaussian curvature is connected with the geodesic curvature of the edge curve by the Gauss-Bonnet theorem, $\int dAK = 2\pi - \oint dsk_g$, where the discretized geodesic curvature is $dsk_g(i) = \pi - \sum_j \theta_j$ [37,38], and θ_j is the interior angle of triangle j incident to i. For the present case of a membrane with a single edge, we have found that a small nonzero Gaussian curvature modulus has little effect on our results. We discard the Gaussian curvature for the following discussion. Therefore, the discretized bending energy E_b is

$$E_b = \frac{\kappa}{2} \sum_{i \in \mathring{\mathcal{M}}} \sigma_i (2H(i))^2, \tag{6}$$

where $\mathring{\mathcal{M}}$ is the interior of triangular mesh $\mathcal{M}$.

Turning now to the edge energy, we write the discretized form $k(i)$ of the edge curvature as

$$k(i) = \frac{\theta_i}{ds(i)}, \tag{7}$$

where θ_i is the angle between bonds i, $(i-1)$ and i, $(i+1)$, and the differential edge length is given by

$$ds(i) = \tfrac{1}{2}(l_{i,i-1} + l_{i,i+1}). \tag{8}$$

with $i-1, i+1$ denoting the neighboring beads of i on the edge.

To construct the discretized geodesic torsion, $\tau_g(i)$, we denote by $\hat{\mathbf{n}}_c(i)$ the surface normal for a bead at the edge, using the same formula (5), as for beads in the interior. Then we define

$$\tau_g(i) = \frac{\vec{\mathbf{r}}_{i+1} - \vec{\mathbf{r}}_{i-1}}{l_{i-1,i+1}} \cdot \left[\hat{\mathbf{n}}_c(i) \times \frac{\hat{\mathbf{n}}_c(i+1) - \hat{\mathbf{n}}_c(i-1)}{2ds(i)} \right]. \tag{9}$$

Thus, the discretized edge energy E_e is given by

$$E_e = \sum_{i \in \partial\mathcal{M}} ds(i) \left\{ \lambda + \frac{B}{2} k^2(i) + \frac{B'}{2} [\tau_g(i) - \tau_g^*]^2 \right\}, \tag{10}$$

where $\partial\mathcal{M}$ is the edge of the triangular mesh $\mathcal{M}$, and the total discretized energy is $E_M = E_b + E_e$.

IV. MONTE CARLO SIMULATIONS: METHODOLOGY AND RESULTS

A. Methodology

To sample the configuration space of the discrete model, we use MC updates for the beads, the bonds, and the edge as shown in Fig. 2. We measure lengths in units of σ_0 and energy in units of $k_B T$. The bead positions are updated by choosing a bead at random and giving it a uniform random translation within a cube of side length $2t$ centered on the bead. Bonds not on the edge are updated by choosing one at random and moving it as shown in Fig. 2 [26]. Bonds on the edge are updated by replacing a single edge bond of a triangle bordering the edge with the two bonds of the same triangle as shown in Fig. 2. Edge bonds can also be updated by reversing this process, replacing two neighboring edge bonds by one and creating a new triangle bordering the edge.

Our simulation should satisfy the condition of detailed balance, $\pi(\mathcal{S})T(\mathcal{S} \to \mathcal{S}') = \pi(\mathcal{S}')T(\mathcal{S}' \to \mathcal{S})$, where $\pi(\mathcal{S}) = \exp[-\beta E(\mathcal{S})]$ is the Boltzmann weight of state $\mathcal{S}$, and $T(\mathcal{S} \to \mathcal{S}')$ is the transition probability from state $\mathcal{S}$ to state $\mathcal{S}'$. To satisfy this condition, we use the Metropolis-Hasting algorithm [39–41], which takes the transition probability to be the product of an acceptance probability $a(\mathcal{S} \to \mathcal{S}')$ and the conditional probability $p(\mathcal{S} \to \mathcal{S}')$ of moving to state $\mathcal{S}'$ given

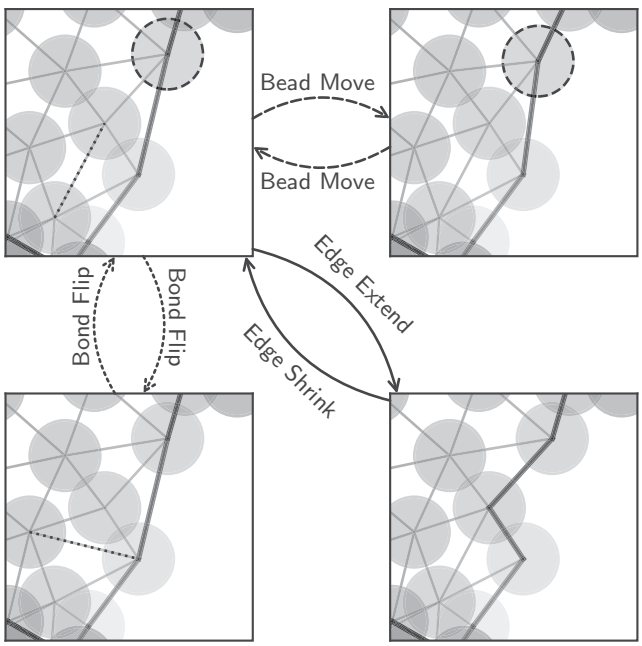

FIG. 2. Monte Carlo updates for the beads, internal bonds, and edge bonds of the membrane. Edge bonds are indicated by a heavy solid line. The updated bead and bond are highlighted with a black dashed line; each update is reversible. The beads have a diameter σ_0 and do not overlap due to hard-core repulsion. The apparent overlap of the beads is due to projection from three to two dimensions; the relative out-of-plane position of the beads and the bonds is represented by the transparency.

that the system is in state $\mathcal{S}$. The acceptance probability is given by

$$a(\mathcal{S} \to \mathcal{S}') = \min\left[1, \frac{\pi(\mathcal{S}')p(\mathcal{S} \to \mathcal{S}')}{p(\mathcal{S}' \to \mathcal{S})\pi(\mathcal{S})}\right]. \quad (11)$$

We have $p(\mathcal{S} \to \mathcal{S}') = p(\mathcal{S}' \to \mathcal{S})$ for bead moves and internal bond flips, since the total numbers of beads and internal bonds before and after these updates remain fixed. However, $p(\mathcal{S} \to \mathcal{S}') \neq p(\mathcal{S}' \to \mathcal{S})$ for edge updates; e.g., if there are L beads on the edge for state $\mathcal{S}$, and $L+1$ for state $\mathcal{S}'$, then $p(\mathcal{S} \to \mathcal{S}') = 1/L$ and $p(\mathcal{S}' \to \mathcal{S}) = 1/(L+1)$.

In the simulation, 1.6×10^5 MC steps are performed for each set of parameters. Each step is composed of N/t^2 attempts at moving a bead chosen at random and N/t^2 attempts at flipping a bond chosen at random. We also make $\sqrt{N}/t^2$ attempts at edge shrinkage or extension. We equilibrate the system for the first 8×10^4 steps. To eliminate the bias introduced by the initial configuration, we start the simulation at a high temperature $\beta = 0.1$ and gradually cool it down by $\delta\beta = 0.1$ for every 4×10^3 steps until it has reached $\beta = 1$, then equilibrate for another 4×10^4 steps, and then record the data for the remaining 8×10^4 steps. The uncertainty in the observables is estimated using Sokal's method [42]. The value $t = 0.2$ is used in updating bead positions. To avoid the formation of a hexatic phase, the maximum bond length is set to $l_0 = 1.56$ [43] and $l_1 = 1.95$ in all of our simulations. We now present the results of our simulations.

B. Disk-to-vesicle transition

We begin by investigating the simple topology change from a disk to a closed vesicle, which is driven by the competition between the line tension and the bending stiffness. For this simulation, we include the line tension as the only edge energy term. Due to advances in computing power over the past two decades, we are able to study membranes with larger bending stiffnesses (or, equivalently, lower temperatures) compared to previous work by Boal and Rao [5]. With their lower value of bending stiffness, Boal and Rao studied the transition from a vesicle to a branched-polymer-like membrane with free edges, with the length of the perimeter scaling like the number of particles N. In our simulations, the bending stiffness can be large enough that the state with free edges is a flat disk, with the length of the perimeter scaling like $N^{1/2}$. We recall that branched-polymer-like shapes are also possible for closed vesicles [44] with a low bending stiffness and high edge tension, but we do not study this phase.

In Fig. 3(a) we plot the average membrane edge length $\langle \int ds \rangle$ (measured in units of σ_0) as a function of the line tension λ for various values of κ, along with pictures of representative membrane configurations. The dotted curve in Fig. 3(a), corresponding to $\kappa = 1$, shows a smooth transition from the branched-polymer shape directly to a closed vesicle. Our result is in quantitative agreement with that of Boal and Rao [5] when setting both bond maximum distances to $l_0 = l_1 = 1.73 \approx \sqrt{3}$. The other curves in Fig. 3(a), corresponding to higher values of the bending stiffness κ, show a smooth transition from the branched polymer shape to a flat disk as the line tension increases and then a sharp transition from the flat disk to a closed vesicle at a higher line tension.

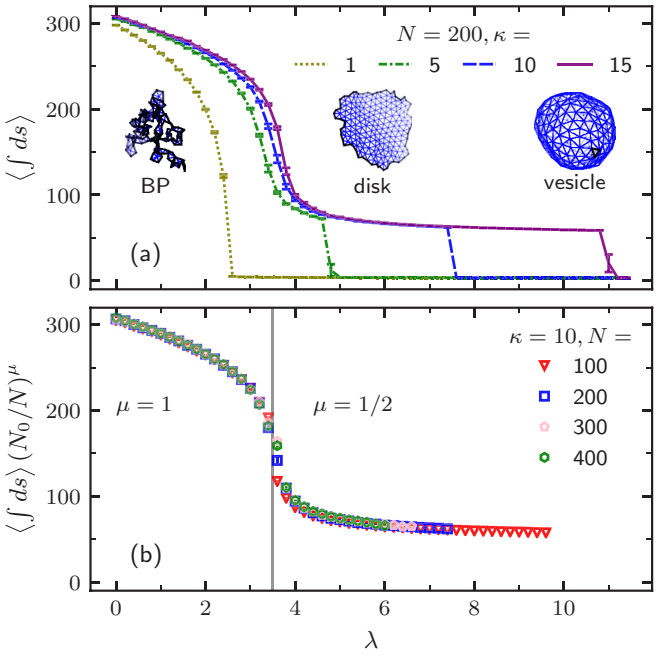

FIG. 3. Simulation results for a membrane with bending stiffness κ (in units of k_BT) and edge tension λ (in units of k_BT/σ_0). All other moduli are 0. (a) Average edge length $\langle \int ds \rangle$ (measured in units of σ_0) as a function of the line tension λ at different κ: $\kappa = 1$ (dashed line), $\kappa = 5$ (dash-dotted line), $\kappa = 10$ (dashed line), and $\kappa = 15$ (solid line). The snapshots of the configurations have $\kappa = 10$ and $\lambda = 2.0$ [self-avoiding branched-polymer (BP) shape], $\lambda = 5.0$ (disk), and $\lambda = 8.0$ (vesicle). (b) Rescaled average edge length vs λ for different system sizes N and $\kappa = 10$, showing the transition from the BP shape to a disk shape. We used $N_0 = 200$ for the rescaling. Note that for each value of N, the rightmost data point is at the value of λ at which the disk transitions to a vesicle.

Figure 3(b) shows how the perimeter scales with N^μ for the case of $\kappa = 10$ and demonstrates the smooth transition from the branched polymer shape ($\mu = 1$) at a lower edge tension λ to the flat disk shape ($\mu = 1/2$) at a higher λ. The possibility of having structures with a fractal dimension where $1/2 < \mu < 1$, particularly near the transition, is not ruled out, but we have not studied such possibilities.

Though the critical line tension for the disk-vesicle transition is sensitive to both the bending stiffness κ and the system size N, the value for λ at the branch-to-disk transition barely changes as κ or N varies. In our study of the effects of chirality in the next section, we take the bending stiffness κ to be large enough that the membrane state with free edges is disklike rather than branched-polymer-like.

C. Edge shape and fluctuation

Next, we add an edge bending stiffness, edge torsional stiffness, and a spontaneous geodesic torsion for the edge. Even in the presence of a line tension λ, the edge of a membrane disk with no edge bending stiffness is jagged, as shown by the branched polymer and disk shapes in Fig. 3(a). Introducing a positive edge bending stiffness B leads to a smoother edge and correlations between the tangent vectors along the edge. Figures 4 and 5 show this effect. In the left panel in

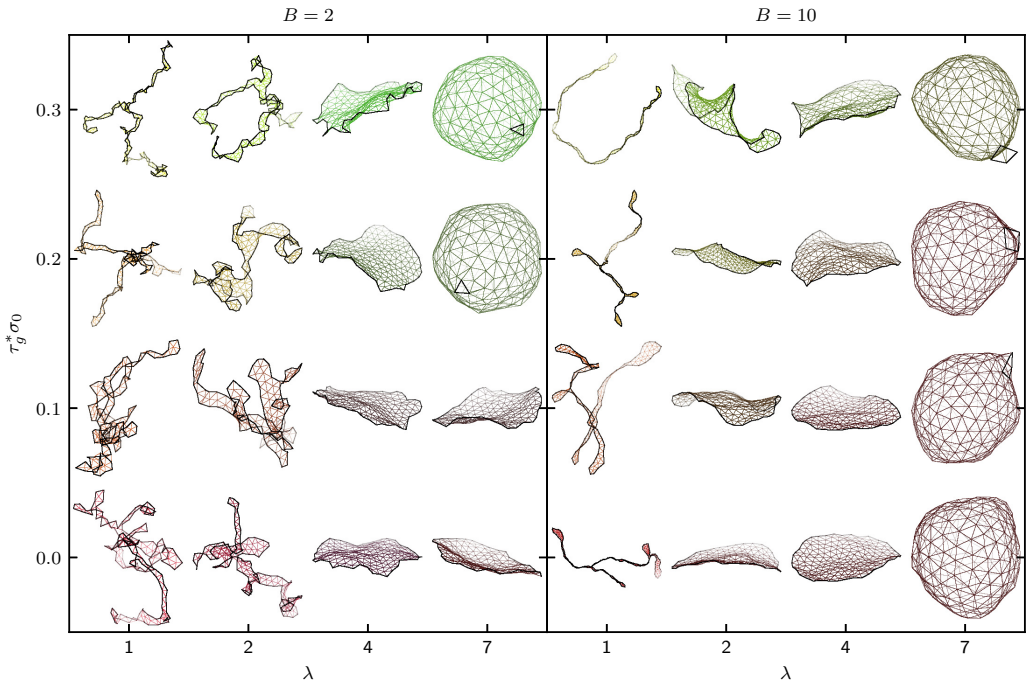

FIG. 4. Snapshots of membranes with various values of the spontaneous edge geodesic torsion τ_g^* for two values of the bending stiffness B; the membranes in the left panel have a low edge bending stiffness, while those on the right have a high edge bending stiffness (B is measured in units of $k_B T \sigma_0$). The system size is $N = 200$, the membrane bending stiffness is $\kappa = 10$ (in units of $k_B T$), and the twist stiffness is $B' = 40$ in units of $k_B T \sigma_0$.

Fig. 4, where $B = 2$, the membranes form branched-polymer shapes for $\lambda = 1, 2$ and disklike shapes with rough edges for $\lambda = 4$. As the spontaneous geodesic torsion τ_g^* of the edge increases, the branches form twisted ribbons. On the other hand, the disk shapes remain mostly flat as τ_g^* increases, but their edges exhibit localized regions of high twisting. These localized regions of twist lead to a rougher edge at the higher values of τ_g^*. In the right panel in Fig. 4, we see that the larger value of the edge bending stiffness leads to a smoother edge. Localized regions of edge twist are suppressed, but the high value of the twist stiffness B' causes the entire membrane to warp like a saddle to allow the edge to twist to a degree that increases with increasing τ_g^*. Note that the high value of the edge bending stiffness B leads to disks with smooth edges even for low values of line tension such as $\lambda = 2$.

Figure 5 displays a quantitative analysis of the membrane shapes. Figure 5(a) shows that the total edge curvature squared decreases rapidly as the stiffness B increases. A nonzero value of the spontaneous geodesic torsion of the edge causes the edge to twist, which necessarily leads to more edge curvature at small values of B. While we recognize that chirality, and, more specifically, handedness, cannot be captured by a single pseudoscalar [45,46], we quantify the handedness of the edge by dividing the average total geodesic torsion of the edge $\langle \int ds \tau_g \rangle$ by the average perimeter $\langle \int ds \rangle$ to associate an average rate of twist with the edge. Figure 5(b) displays the average rate of twist of the edge vs the edge stiffness for various values of the spontaneous geodesic torsion τ_g^* and a large value of the twist modulus B'. When $\tau_g^* = 0$, there is no preference for either handedness, and the average rate of twist vanishes. For nonzero τ_g^* and small B, the edge twists at a rate that is close to the spontaneous geodesic torsion because B' is so large that the cost for departure of τ_g from τ_g^* is high. But since twist of the edge requires curvature of the edge, the average twist decreases as B increases. Varying the twist stiffness B' affects τ_g more directly. Lowering B' leads to a smaller value of τ_g. As B' approaches 0, τ_g likewise approaches 0, as there is no energy cost related to chirality. By their nature, achiral membranes have no preference to twist either left-handed or right-handed.

Figures 5(c) and 5(d) show the correlation function $g(m) = \langle \hat{\mathbf{n}}_c(0) \cdot \hat{\mathbf{n}}_c(m) \rangle = (1/L) \sum_{i=0}^{L-1} \hat{\mathbf{n}}_c(i) \cdot \hat{\mathbf{n}}_c(i+m)$ of the surface normal vector $\hat{\mathbf{n}}_c$ at the edge for the chiral and achiral cases, respectively, for various values of the edge bending stiffness B. When $B = 0$, the correlation function decays rapidly since the edge is jagged. If $B = 0$ but the membrane edge has a spontaneous geodesic torsion, the localized twist regions of the edge lead to less correlation than in the achiral case. As B increases, the correlation function for the chiral case starts to develop oscillations since the entire membrane is twisting like a potato chip.

We have also studied the power spectrum of the edge fluctuations [17]. By following the membrane edge position $\vec{\mathbf{r}}_c(i)$, the distance from an edge bead i to the averaged membrane center can be calculated as $r(i) = |\vec{\mathbf{r}}_c(i) - \langle \vec{\mathbf{r}}_c \rangle|$. The autocorrelation of edge fluctuations is given by $\langle \delta r(0) \delta r(m) \rangle = \langle r(0) r(m) \rangle - \langle r(0) \rangle^2$, where $\delta r(i) = r(i) - \langle r(0) \rangle$ is the deviation of $r(i)$ from the average membrane radius. Thus the power spectrum is the cosine transform of the autocorrelation function $\langle \delta r_q \delta r_{-q} \rangle = 2 \sum_m \langle \delta r(0) \delta r(m) \rangle \cos[q(m + 1/2)]$.

Figure 6(a) shows the normalized power spectrum $\langle \delta r_q \delta r_{-q} \rangle (q \langle L \rangle)^2$ of edge fluctuations for various values of the spontaneous geodesic torsion τ_g^*. A peak in the middle of the curves appears and grows as τ_g^* increases, which is also

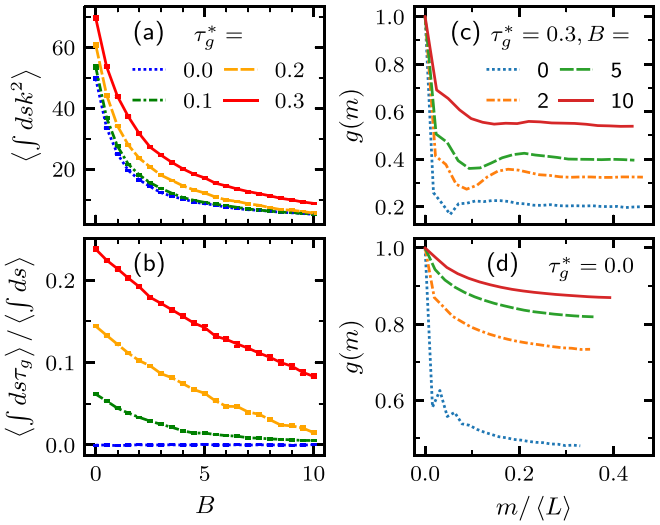

FIG. 5. Geometrical properties of the membrane edge in the disk region of the phase diagram for a membrane with $N = 200$, $\kappa = 10$, $\lambda = 4$, and torsional stiffness $B' = 40$ (measured in units of $k_BT\sigma_0$). (a) The average total square curvature (measured in units of σ_0^{-1}) vs B (measured in units of $k_BT\sigma_0$) for $\tau_g^* = 0$ (dotted line), $\tau_g^* = 0.1$ (dash-dotted line), $\tau_g^* = 0.2$ (dashed line), and $\tau_g^* = 0.3$ (solid line). (b) Average total geodesic torsion per average perimeter versus B, with the legend the same as in (a). (c) The correlation function $g(m) = \langle \hat{\mathbf{n}}_c(0) \cdot \hat{\mathbf{n}}_c(m) \rangle$ of the surface normal vector $\hat{\mathbf{n}}_c$ along the edge versus the distance along the edge measured in terms of the number of beads m divided by the averaged number of beads on the edge $\langle L \rangle$ for $\tau_g^* = 0.3$ and $B = 0$ (dotted line), $B = 2$ (dash-dotted line), $B = 5$ (dashed line), and $B = 10$ (solid line). The oscillation of $g(m)$ indicates the twist of the edge. (d) The edge normal-normal correlation function $g(m)$ along the edge for the achiral case where $\tau_g^* = 0$. The legend is the same as in (c).

observed in experiments [17]. Increasing the edge bending stiffness B flattens the curve and makes this phenomenon less detectable. Figure 6(b) shows the configurations for several different values of τ_g^*. As τ_g^* increases, the membrane edge becomes more rippled, which is also in qualitative agreement with experiment [3]. The detailed dependence of the peak on the chiral coupling follows from the equipartition theorem, as described in [17]. Note that the theoretical peak in [17] is sharper than in Fig. 6(a) because the line tension is fit to the measurements and shown to reduce with increasing chirality in [17], whereas here we keep the line tension fixed.

D. Ribbon formation under external force

Experiments show that a colloidal membrane disk subject to a stretching force by laser tweezers deforms into a twisted ribbon, with the twist increasing as the ends of the membrane are drawn apart [3,27]. Motivated by this work, we fix the distance between two beads on the edge of our membrane and find the shape as a function of the distance l_f between these two beads. As the distance increases, the membrane forms a twisted ribbon, with the twist increasing with distance, as shown in Fig. 7(a). Note that a helicoid with right-handed helical edges has a positive geodesic torsion, in accord with the fact that we find right-handed ribbons when we pull on a

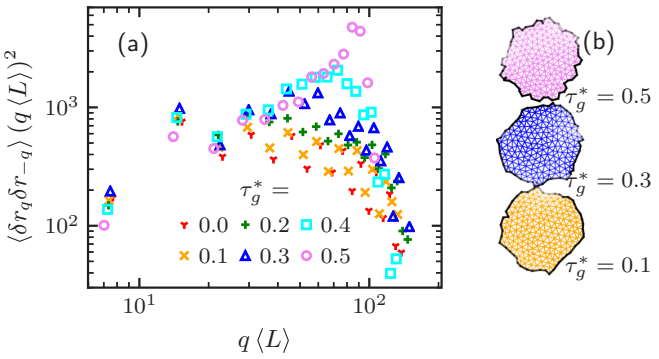

FIG. 6. Edge fluctuations of the membrane for various values of the spontaneous geodesic torsion. The parameters are such that the membrane forms a disk with a larger value of the line tension: $N = 200$, $\kappa = 15$, $\lambda = 7$, $B = 0$, and $B' = 40$. (a) Normalized power spectrum $\langle \delta r_q \delta r_{-q} \rangle (q\langle L \rangle)^2$ calculated from the cosine transform of the edge fluctuations (measured from the center of the membrane) as a function of the corresponding wave number q times the averaged number of beads on the edge $\langle L \rangle$. (b) Snapshots of membrane configurations with $\tau_g^* = 0.1$, 0.3, and 0.5, from bottom to top.

membrane disk with positive τ_g^*. If we reverse the sign of τ_g^*, then we find that the handedness of the ribbons reverses as shown in Fig. 8.

The average twist rate of the ribbon increases roughly linearly with extension l_f, except when $\tau_g^* = 0$, in which case the

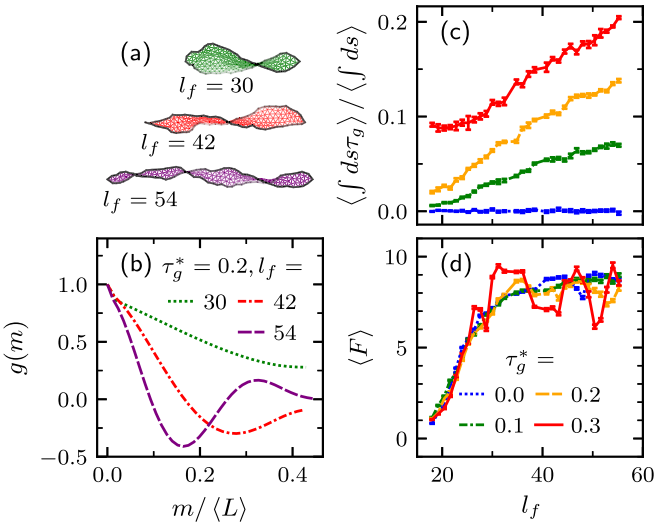

FIG. 7. Results for a membrane under external forces. The parameters are such that the membrane forms a disk in the absence of external force: $N = 200$, $\kappa = 10$, $\lambda = 4$, $B = 10$, and $B' = 40$. (a) Snapshots of the membrane with $\tau_g^* = 0.2$ and, from top to bottom, $l_f = 30$, 42, and 54. (b) Correlation function $g(m)$ for the surface normal at the edge versus the distance along the edge measured in terms of the number of beads m divided by the average number of beads on the edge $\langle L \rangle$, for $l_f = 30$ (dotted line), $l_f = 42$ (dash-dotted line), and $l_f = 54$ (dashed line). (c) Average total geodesic torsion divided by the average perimeter for $\tau_g^* = 0$, 0.1, 0.2, and 0.3, from bottom to top. (d) Force required to impose the separation l_f, calculated as the derivative of the total average energy $\langle E \rangle$ with respect to l_f, for $\tau_g^* = 0$ (dotted line), $\tau_g^* = 0.1$ (dash-dotted line), $\tau_g^* = 0.2$ (dashed line), and $\tau_g^* = 0.3$ (solid line).

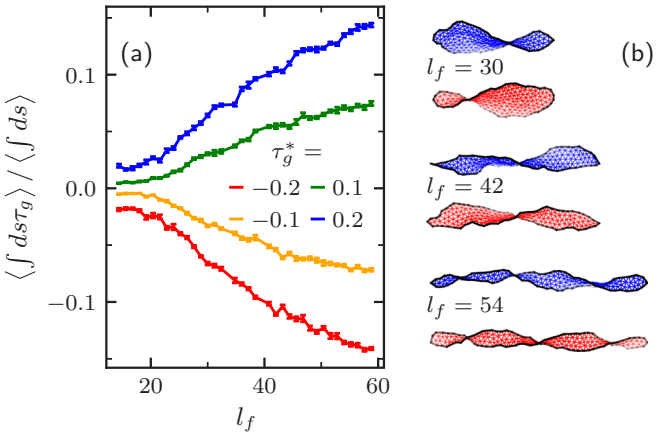

FIG. 8. The effect of the sign of the spontaneous geodesic torsion of the edge on the shape of a membrane subject to an external force, with parameters $N = 200$, $\kappa = 10$, $\lambda = 4$, $B = 10$, and $B' = 40$. (a) Average total geodesic torsion divided by the average perimeter for $\tau_g^* = 0.2, 0.1, -0.1$, and -0.2, from top to bottom. (b) Snapshots of a membrane with $\tau_g^* = 0.2$ (first, third, and fifth from the top) and $\tau_g^* = -0.2$ (second, fourth, and sixth from the top), showing that membranes with opposite τ_g^* have opposite handedness, for $l_f = 30$, 42, and 54 for the pairs from top to bottom.

membrane does not twist. (Recall that we have set $\bar{\kappa} = 0$, so the membrane bending energy does not give a tendency for the membrane to have a negative Gaussian curvature). Figure 7(b) shows the correlation function $g(m)$ for the membrane normal at the edge. The increase in oscillations with increasing values of l_f correspond to an increase in membrane twist with l_f. Finally, Fig. 7(d) shows the force required to hold the beads at separation l_f. The force is found by calculating the average energy as a function of l_f and then differentiating with respect to l_f. The force increases linearly and then asymptotes to a constant value, 2λ. As τ_g^* increases, the value of the force plateau decreases. Similar results were found in a semianalytic model which assumed that the shape of the membrane is a helicoid [27].

V. CONCLUSION

Colloidal membranes take on a wide range of shapes beyond flat disks and closed vesicles due to their tendency to have free edges and due to the chirality of their constituent particles. In this article, we determined the membrane shapes and their properties using Monte Carlo simulations with an effective energy that accounts for the liquid crystalline degrees of freedom near the edge using geometric properties of the edge. Our work extends semianalytical approaches that make simplifying assumptions about the membrane shape [27]. The presence of the edges and the effective energy terms such as the edge bending stiffness and edge torsional stiffness lead to a richer free energy landscape compared to existing studies of systems either with no edge [25,47] or with only line tension and bending stiffness [5,9]. Although we use a simple effective model that does not account for the liquid crystalline degrees of freedom in the membrane bulk, the shapes we find are qualitatively similar to the ribbons [27], vesicles [48], and saddle shapes [49] found in experiments. Also, we have disregarded the Gaussian curvature term since experimental measurements show that $\bar{\kappa} \ll \kappa$ [17,19,30]. In our Monte Carlo studies, we have found that a small nonzero Gaussian curvature modulus has little effect on our results. Finally, future work should test the validity of the assumptions of the effective theory by explicitly accounting for the liquid crystalline degrees of freedom in Monte Carlo simulations of the membrane.

ACKNOWLEDGMENTS

Helpful discussions with A. Balchunas, L. L. Jia, M. Zakhary, and Z. Dogic are gratefully acknowledged. This work was supported in part by the National Science Foundation through Grants No. CMMI-1634552 and No. MRSEC-1420382.

[1] U. Seifert, Adv. Phys. **46**, 13 (1997).
[2] E. Barry and Z. Dogic, Proc. Natl. Acad. Sci. USA **107**, 10348 (2010).
[3] T. Gibaud, E. Barry, M. J. Zakhary, M. Henglin, A. Ward, Y. Yang, C. Berciu, R. Oldenbourg, M. F. Hagan, D. Nicastro *et al.*, Nature **481**, 348 (2012).
[4] M. J. Zakhary, T. Gibaud, C. N. Kaplan, E. Barry, R. Oldenbourg, R. B. Meyer, and Z. Dogic, Nat. Commun. **5**, 3063 (2014).
[5] D. H. Boal and M. Rao, Phys. Rev. A **46**, 3037 (1992).
[6] L. V. Chernomordik and M. M. Kozlov, Nat. Struct. Mol. Biol. **15**, 675 (2008).
[7] C. Huang, D. Quinn, Y. Sadovsky, S. Suresh, and K. J. Hsia, Proc. Natl. Acad. Sci. USA **114**, 2910 (2017).
[8] P. Fromherz, Chem. Phys. Lett. **94**, 259 (1983).
[9] S.-J. Zhao and J. Kindt, Europhys. Lett. **69**, 839 (2005).
[10] A. Saithoh, K. Takiguchi, Y. Tanaka, and H. Hotani, Proc. Natl. Acad. Sci. USA **95**, 1026 (1998).
[11] Z. C. Tu and Z. C. Ou-Yang, Phys. Rev. E **68**, 061915 (2003).
[12] T. G. Barclay, K. Constantopoulos, and J. Matisons, Chem. Rev. **114**, 10217 (2014).
[13] J. V. Selinger, M. S. Spector, and J. M. Schnur, J. Phys. Chem. B **105**, 7157 (2001).
[14] C. N. Kaplan, H. Tu, R. A. Pelcovits, and R. B. Meyer, Phys. Rev. E **82**, 021701 (2010).
[15] H. Tu and R. A. Pelcovits, Phys. Rev. E **87**, 032504 (2013).
[16] H. Tu and R. A. Pelcovits, Phys. Rev. E **87**, 042505 (2013).
[17] L. L. Jia, M. J. Zakhary, Z. Dogic, R. A. Pelcovits, and T. R. Powers, Phys. Rev. E **95**, 060701(R) (2017).
[18] L. Kang, T. Gibaud, Z. Dogic, and T. Lubensky, Soft Matter **12**, 386 (2016).
[19] T. Gibaud, C. N. Kaplan, P. Sharma, M. J. Zakhary, A. Ward, R. Oldenbourg, R. B. Meyer, R. D. Kamien, T. R. Powers, and Z. Dogic, Proc. Natl. Acad. Sci. USA **114**, E3376 (2017).
[20] Y. Yang, E. Barry, Z. Dogic, and M. F. Hagan, Soft Matter **8**, 707 (2012).

[21] S. Xie, R. A. Pelcovits, and M. F. Hagan, Phys. Rev. E **93**, 062608 (2016).
[22] P. G. de Gennes, Sol. State Commun. **10**, 753 (1972).
[23] M. Kléman, *Points, Lines, and Walls* (John Wiley & Sons, Chichester, UK, 1983).
[24] G. Gompper and D. Kroll, J. Phys.: Condens. Matter **9**, 8795 (1997).
[25] G. Gompper and D. Kroll, in *Statistical Mechanics of Membranes and Surfaces* (World Scientific, Singapore, 2004), pp. 359–426.
[26] A. Baumgärtner and J.-S. Ho, Phys. Rev. A **41**, 5747 (1990).
[27] A. Balchunas, L. L. Jia, M. J. Zakhary, J. Robaszewski, T. Gibaud, Z. Dogic, R. A. Pelcovits, and T. R. Powers, Phys. Rev. Lett. **125**, 018002 (2020).
[28] P. B. Canham, J. Theor. Biol. **26**, 61 (1970).
[29] W. Helfrich, Z. Naturforsch. C **28**, 693 (1973).
[30] A. J. Balchunas, R. A. Cabanas, M. J. Zakhary, T. Gibaud, S. Fraden, P. Sharma, M. F. Hagan, and Z. Dogic, Soft Matter **15**, 6791 (2019).
[31] D. J. Struik, *Lectures on Classical Differential Geometry* (Courier Corp., North Chelmsford, MA, 1961).
[32] C. Itzykson, in *Proceedings GIFT Seminar, Jaca 85*, edited by M. A. J. Abad and A. Cruz (World Scientific, Singapore, 1986), pp. 130–188.
[33] C. Itzykson and J.-M. Drouffe, *Statistical Field Theory, Vol. 2* (Cambridge University Press, Cambridge, UK, 1989).
[34] D. Espriu, Phys. Lett. B **194**, 271 (1987).
[35] M. Meyer, M. Desbrun, P. Schröder, and A. H. Barr, in *Visualization and Mathematics III* (Springer, Berlin, 2003), pp. 35–57.
[36] K. Crane, F. de Goes, M. Desbrun, and P. Schröder, in *ACM SIGGRAPH 2013 Courses*, *SIGGRAPH '13* (ACM Press, New York, 2013).
[37] M. Jin, J. Kim, and X. D. Gu, *Discrete Surface Ricci Flow: Theory and Applications*, edited by R. Martin, M. Sabin, and J. Winkler, Mathematics of Surfaces XII. Mathematics of Surfaces 2007. Lecture Notes in Computer Science Vol. 4647 (Springer, Berlin, Heidelberg, 2007).
[38] M. M. Mesmoudi, L. De Floriani, and P. Magillo, in *International Workshop on Applications of Discrete Geometry and Mathematical Morphology* (Springer, Berlin, 2010), pp. 28–42.
[39] W. Krauth, *Statistical Mechanics: Algorithms and Computations*, *Vol. 13* (Oxford University Press, Oxford, UK, 2006).
[40] W. K. Hastings, Biometrika **57**, 97 (1970).
[41] N. Metropolis, A. W. Rosenbluth, M. N. Rosenbluth, A. H. Teller, and E. Teller, J. Chem. Phys. **21**, 1087 (1953).
[42] A. Sokal, in *Functional Integration* (Springer, Berlin, 1997), pp. 142–145.
[43] G. Gompper and D. M. Kroll, Eur. Phys. J. E **1**, 153 (2000).
[44] D. M. Kroll and G. Gompper, Science **255**, 968 (1992).
[45] A. B. Harris, R. D. Kamien, and T. C. Lubensky, Rev. Mod. Phys. **71**, 1745 (1999).
[46] E. Efrati and W. T. M. Irvine, Phys. Rev. X **4**, 011003 (2014).
[47] T. Kohyama, D. M. Kroll, and G. Gompper, Phys. Rev. E **68**, 061905 (2003).
[48] J. Robaszewski, L. Jia, T. R. Powers, R. A. Pelcovits, and Z. Dogic (unpublished).
[49] P. Sharma, L. Saikia, A. Khanra, and Z. Dogic (unpublished).